Effects on Retinal Stimulation of the Geometry and the Insertion Location of Penetrating Electrodes

Yunseo Son, *Member, IEEE*, Zhijie Charles Chen, *Student Member, IEEE*, Hyeonhee Roh, *Student Member, IEEE*, Byung Chul Lee, *Member, IEEE*, and Maesoon Im, *Member, IEEE*

***Abstract*— Retinal implants have been developed and implanted to restore vision from outer retinal degeneration, but their performance is still limited due to the poor spatial resolution. To improve the localization of stimulation, microelectrodes in various three-dimensional (3D) shapes have been investigated. In particular, computational simulation is crucial for optimizing the performance of a novel microelectrode design before actual fabrication. However, most previous studies have assumed a uniform conductivity for the entire retina without testing the effect of electrodes placement in different layers. In this study, we used the finite element method to simulate electric fields created by 3D microelectrodes of three different designs in a retina model with a stratified conductivity profile. The three electrode designs included two conventional shapes - a conical electrode (CE) and a pillar electrode (PE); we also proposed a novel structure of pillar electrode with an insulating wall (PEIW). A quantitative comparison of these designs shows the PEIW generates a stronger and more confined electric field with the same current injection, which is preferred for high-resolution retinal prostheses. Moreover, our results demonstrate both the magnitude and the shape of potential distribution generated by a penetrating electrode depend not only on the geometry, but also substantially on the insertion depth of the electrode. Although epiretinal insertions are mainly discussed, we also compared results for subretinal insertions. The results provide valuable insights for improving the spatial resolution of retinal implants using 3D penetrating microelectrodes and highlight the importance of considering the heterogeneity of conductivities in the retina.**

***Index Terms*— Artificial vision, retinal implant, retinal prosthesis, computational simulation, penetrating electrodes.**

Manuscript received 20 June 2023; revised 8 August 2023; accepted 14 September 2023. Date of publication 20 September 2023; date of current version 28 September 2023. This work was supported in part by the Korea Institute of Science and Technology (KIST) under Grant 2E32551; and in part by the National Research Foundation of Korea (NRF) funded by the Korean Government [Ministry of Science and ICT (MSIT)] under Grant 2020R1C1C1006065, Grant 2021M3F3A2A01037366, Grant 2022M3E5E8017395, and Grant RS-2023-00302397. *(Corresponding author: Maesoon Im.)*

Yunseo Son is with the Brain Science Institute, Korea Institute of Science and Technology, Seoul 02792, South Korea, and also with the Department of Electrical and Biological Physics, Kwangwoon University, Seoul 01897, South Korea.

Zhijie Charles Chen is with the Department of Electrical Engineering, Stanford University, Stanford, CA 94305 USA.

Hyeonhee Roh is with the Brain Science Institute, Korea Institute of Science and Technology, Seoul 02792, South Korea, and also with the School of Electrical Engineering, College of Engineering, Korea University, Seoul 02841, South Korea.

Byung Chul Lee is with the Bionics Research Center, Korea Institute of Science and Technology, Seoul 02792, South Korea, also with the Division of Bio-Medical Science and Technology, KIST School, University of Science and Technology (UST), Seoul 02792, South Korea, and also with the KHU-KIST Department of Converging Science and Technology, Kyung Hee University, Seoul 02447, South Korea.

Maesoon Im is with the Brain Science Institute, Korea Institute of Science and Technology, Seoul 02792, South Korea, also with the Division of Bio-Medical Science and Technology, KIST School, University of Science and Technology (UST), Seoul 02792, South Korea, and also with the KHU-KIST Department of Converging Science and Technology, Kyung Hee University, Seoul 02447, South Korea (e-mail: maesoon.im@kist.re.kr).

Digital Object Identifier 10.1109/TNSRE.2023.3317496

I. Introduction

VISUAL perception begins from the photoreceptors in the retina. The photoreceptors convert light into nerve signals and transmit the information to the downstream neurons such as bipolar cells and ganglion cells. These light-sensing neurons can be irreversibly damaged and/or lost by outer retinal degenerative diseases including age-related macular degeneration (AMD) [1], [2] and retinitis pigmentosa (RP) [3], [4], [5]. Patients of those diseases experience gradual vision impairment and may eventually lose their sight [6], [7]. Fortunately, other inner retinal neurons are known to survive those ailments [8], [9], making them the viable target of electrical stimulation to evoke visual perception in blind individuals again [10], [11], [12]. Several retinal prosthetic devices had been developed and commercialized around the world: Argus II (Second Sight) [11], [13], [14], [15] and Alpha IMS/AMS (Retina Implant) [5], [16] are the two representative examples. Among other prosthetic devices which had proceeded to clinical trials [17], [18], [19], [20], PRIMA (Pixium Vision) has recently demonstrated the highest prosthetic acuity to date, 20/438 [19], [20]. However, this level of visual acuity is still far below even the legal limit of blindness in the United States (20/200). Toward matching the acuity of healthy natural vision (20/20), the primary challenge for prosthetic

vision is thought to be the poor spatial confinement of electric stimulation [21], [22], [23]. To address this issue, numerous researches proposed non-planer electrode designs such as three-dimensional wells [24], concave/convex hemispherical/conical shapes [25], cylindrical pillar [26], [27], honeycomb structures [28], and microneedles [29], [30], [31]. Also, penetrating electrodes can be used to reduce the distance between the stimulation site and the target cells to improve the stimulation strength [35]. In addition to the various electrode shapes, the integration of a local return electrode around each active electrode was found effective in stimulation current confinement and thereby minimizing cross-talk [28].

Prior to electrode fabrication, computational simulation is often used to test the efficacy of new electrode designs in terms of spatial properties of electric stimulation including localization. Most such studies simplified the model by assigning a homogeneous electrical conductivity to the multi-layer retina [10], [24], [26], [28], [33], [34], [35]. In reality, however, the retina is known to have heterogeneous conductivities in different layers [25], [36], [37], [38], [39], [40], [41], [42], [43], [44]. This discrepancy may render the electric stimulation outcome substantially inaccurate, particularly with the variability of the electrode penetration depth in the retina. The effect of insertion depth has not been well examined in consideration of the conductivity heterogeneity.

In this study, we investigated the electrical response of the retina to current stimulation applied by penetrating electrodes located at various depths of the intraretinal space using a finite element method (FEM) simulation tool. To explore the effect of electrode shapes on spatial properties of the electric field, we compared the simulation results from three different designs of the electrode geometry. We first simulated the electric fields for epiretinally inserted electrodes of all three designs. Then, to investigate potential differences depending on insertion direction, we compared the results between both epiretinal and subretinal insertions for the two electrode designs which produced stronger electric fields.

II. Methods

A. Computational Model

The computational models were constructed, and their electric fields were computed with an FEM software, COMSOL Multiphysics 5.2 (COMSOL AB, Stockholm, Sweden). We used the electrostatic module to solve the Poisson equation of volumetric conduction for electric potential, assuming a steady-state electric field. Figure 1A illustrates our simulation model that consists of, from the top to the bottom, a distant ground plane, a vitreous body (VB), a microelectrode inside the retina. Two cylindrical volumes were defined for the VB and the retina (Fig. 1Ai), both which had a diameter of 18,000 μm; the thickness of the retina was 332 μm, and the total (*i.e.*, VB and retina) height was 18,000 μm. The total size of a realistic human retina was estimated to have a radius of over 18,000 μm [45]. However, to make the model computationally efficient, we created a model with a radius of 9,000 μm.

Mesh sizes were differentially defined: loose and dense meshes were used for the VB and the retina areas, respectively (Figs. 1Bi vs. 1Bii). In the simulation, the basic mesh size was "Finer". However, because of the minute features of sharp electrodes, specifically around the tip of a cone, the meshing size in some domains was set as "Extra fine" or "Extremely fine". To enhance the accuracy of our calculation, we included an additional cylindrical layer engulfing the electrodes where a denser mesh was used (indicated by an arrow with 'Finer mesh' in the inset of Fig. 1Aii). In the present study, we used stationary solutions of the COMSOL simulation.

B. Electrode Models in Three Different Shapes

We simulated three types of penetrating electrodes (Fig. 1C): 1) a conical electrode (CE), 2) a pillar electrode (PE), and 3) a pillar electrode with an insulating wall (PEIW) of 132 μm in height (but for CE, height is 151 μm. See Results). In particular, we introduced the PEIW which may enhance the confinement of electric stimulation with the insulating wall surrounding a current-injection surface (hereafter simply referred to as current source) by physically blocking current spread. The earlier studies already attempted to use wall structures but some portion of the wall structure was conductive and hard-wired to ground (so called 'local ground electrodes') [26], [28]. This may increase the complexity of fabrication processes. Instead, we tested the efficacy of an electrically passive wall without grounding.

The surface areas of the current source (highlighted in pink in Fig. 1C) were controlled in all electrodes to be 100 $\pi\,\mu m^2$ with the "floating potential" boundary condition in COMSOL. To make the surface area identical, we used a base radius of 10 μm in common for both the PE and the CE while the PEIW had a base radius of 15 μm. The insulating wall length of PEIW was set to be 7 μm, and the wall thickness was set to be 5 μm. The rest of the surfaces were insulated with the "insulating current" boundary condition. In this study, we chose to set the stimulation current at 100 nA. This is because the main focus was on comparing potential outcomes to find optimal condition, without excessive emphasis on their specific magnitudes.

C. Simulation of Epiretinal and Subretinal Stimulation

The retina model comprised 8 distinct layers (Fig. 1D): nerve fiber layer (NFL), ganglion cell layer (GCL), inner plexiform layer (IPL), inner nuclear layer (INL), outer plexiform layer (OPL), outer nuclear layer (ONL), outer segment (OS) of photoreceptors, and retinal pigment epithelium (RPE). Both electrical conductivities and thicknesses of those layers were adapted from a recent publication [25], the values of which were shown in the caption of Fig. 2. Unlike previous simulation studies [28], [35], we used a normal retina rather than a degenerate one in our simulations because the layer-by-layer conductivity information is unavailable for a degenerate retina which may have different values due to the substantial reorganization and loss of retinal neurons [46]. Our understanding in the healthy retina structure may be further extended to the degenerate retina if conductivity changes are precisely characterized later.

In the case of outer retinal degeneration, the layers housing photoreceptors are subjected to considerable damage, leading

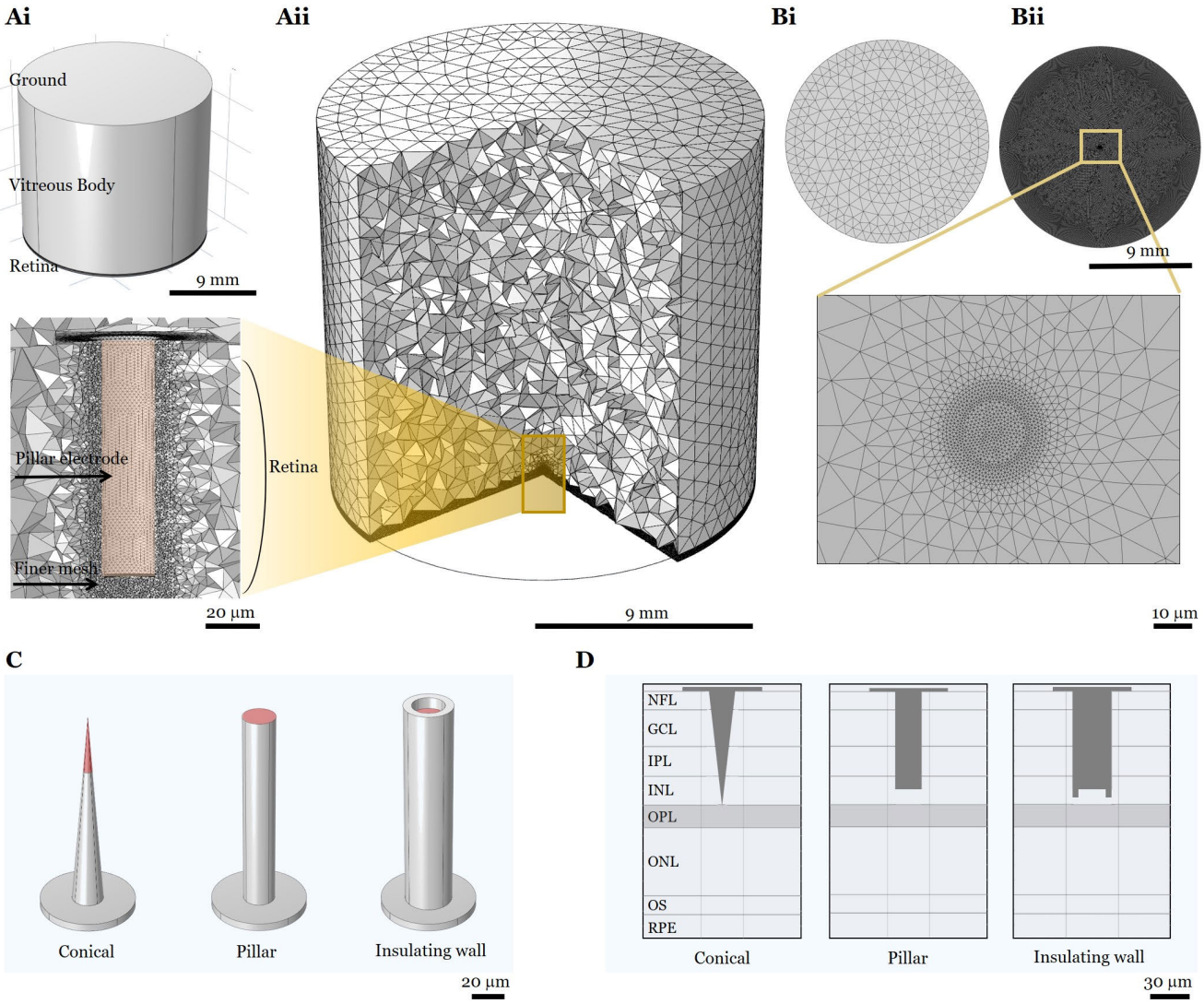

Fig. 1. Three types of penetrating microelectrode structures and the meshing for computation. **(Ai)** The entire simulated domain **(Aii)** Meshing in the retina and vitreous body (VB) model. The inset shows the detailed meshing around the electrode. **(Bi)** Mesh at the surface of VB. **(Bii)** Mesh at the surface of retinal pigment epithelium (RPE). The mesh was finer to precisely compute electrical potential distribution. **(C)** 3D schematics of the three electrode designs studied. Electrically active surfaces marked in pink, the areas of which are the same in all three designs. **(D)** Cross-sectional views of the electrodes inserted to the middle of the INL. NFL: nerve fiber layer, GCL: ganglion cell layer, IPL: inner plexiform layer, INL: inner nuclear layer, OPL: outer plexiform layer, ONL: outer nuclear layer, OS: outer segment of photoreceptors, RPE: retinal pigment epithelium.

to significant alterations in thickness or conductivity. Nevertheless, the layers we located the electrodes in the present study (*i.e.*, OPL, INL, IPL, GCL, and NFL) are known to be remained less scathed [12], [46]. Thus, minor deviations from our results that utilized conductivity values of normal retinas may be shown in the real stimulation tests using degenerate retinas at the early stage of diseases.

Retinal implants can be placed at either epiretinal [3], [11], [13], [14], [15], [47] or subretinal [16], [48], [49] spaces. Therefore, we simulated cases when the three types of penetrating electrodes were inserted from either size (Figure 2).

III. Results

A. Electric Stimulation Was Most Effectively Confined by the Pillar Electrode With an Insulating Wall (PEIW)

Surgical placement of microelectrodes from the epiretinal side is easier than that from the subretinal side [50], [51]. On the other hand, our simulation results obtained from the penetrating electrodes inserted from the epiretinal and subretinal sides were largely similar in terms of the spatial properties of electric field in horizontal directions at a given plane of retinal layers (Fig. 6 and Results D), with a slight difference in the vertical direction. Therefore, we primarily report here the results from the epiretinal insertion.

At the advanced stage of retinal degeneration, photoreceptors disappear and bipolar cells retract their dendrite [52], leaving INL as the furthest layer from the epiretinal side. Thus, for the PE and the PEIW, the electrode surfaces were positioned at the middle of the INL. Because the current starts diverging from the top of the sidewall in the CE configuration, the middle of the electrode tip was positioned at the middle of INL (Fig. 3Ai). Electrical potentials produced by 100 nA current application were visualized in cross-sectional views (Figs. 3Ai, 3Bi, and 3Ci) Note that the color bar ranges for

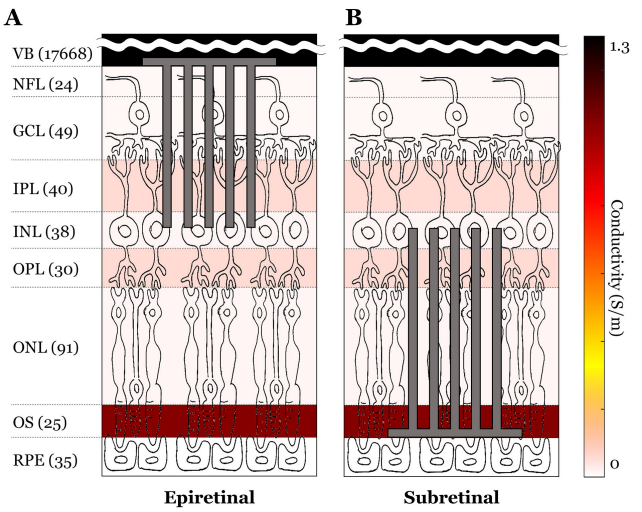

Fig. 2. The retina model was composed of several layers with different conductivities. **(A)** Schematical view of pillar electrodes inserted from epiretinal side. **(B)** Same as ***A*** but for subretinal insertion. Retinal layers used for the simulation were, from the top, vitreous body (VB), nerve fiber layer (NFL), ganglion cell layer (GCL), inner plexiform layer (IPL), inner nuclear layer (INL), outer plexiform layer (OPL), oute nuclear layer (ONL), outer segment (OS) of photoreceptors, and retinal pigment epithelium (RPE). The conductivities (in S/m) of each layer were 1.2821, 0.0126, 0.0126, 0.0571, 0.0147, 0.0571, 0.0147, 1.0309 and 0.001 in the same order; the background (*i.e.,* underneath the cartoon of cells) color of each layer indicates the conductivity as shown in the legend at right. The thicknesses (μm) were 17668, 24, 49, 40, 38, 30, 91, 25, and 35 as noted in parentheses next to the layer names.

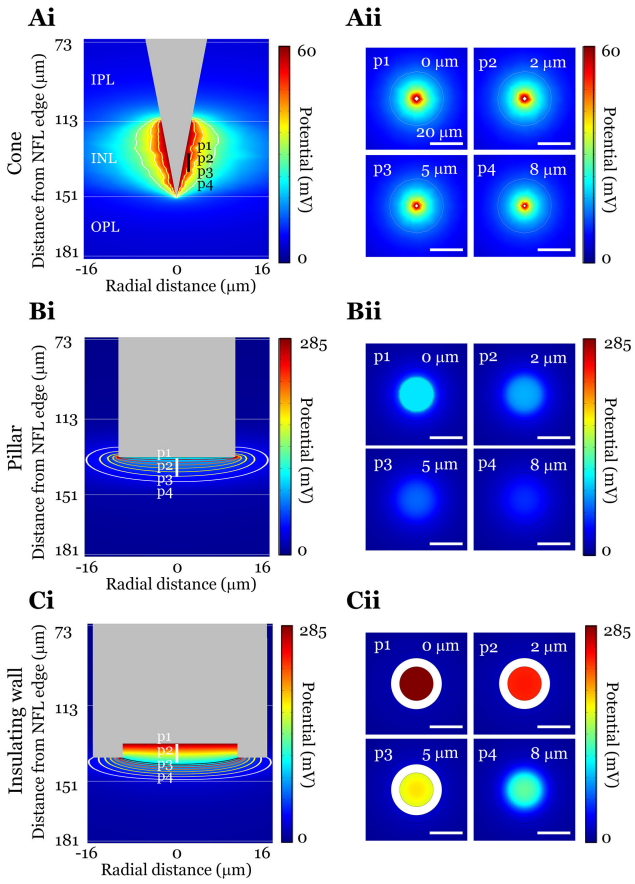

Fig. 3. Electric field generated by a pillar electrode with an insulating wall (PEIW) was the strongest and most spatially confined. **(Ai)** Cross-sectional view of the potential distribution when 100 nA was applied to a conical electrode (CE) inserted in the middle of the INL. Solid lines represent equipotential contour lines drawn from 30 mV at the outermost curve, with 10 mV increments inside. The inner layers are 40 mV and 50 mV. **(Aii)** Top views of the potential distributions at the planes (p1-p4) which were 0, 2, 5, and 8 μm away from the current source, respectively. **(Bi** and **Bii)** Same as ***Ai*** and ***Aii*** but for a pillar electrode (PE). **(Ci** and **Cii)** Same as ***Ai*** and ***Aii*** but for a PEIW. The white rings in the first 3 planes are the insulation wall with an undefined potential. For the equipotential lines of PE and PEIW, they are represented from 30 mV to 100 mV with 10 mV increments. Note that the scale of color legend in panels ***(Ai)*** and ***(Aii)*** is different from other panels because the maximum potential values were significantly smaller for the CE.

PE and PEIW were adjusted to match that of the PEIW, while the range for CE was different from those of PE and PEIW. We also plotted potentials at four different locations: *p1-p4* were horizontal planes 0, 2, 5, and 8 μm away from the electrode surface (Fig. 3). In the case of the CE, the surface of the midpoint of the current source was set as 0 μm, and measurements were taken at positions away from that reference point in the subretinal direction. In both vertical and horizontal directions, CE and PEIW created the smallest and the largest electric potential, respectively (*compare* Figs. 3A vs. 3C). At 2 μm away from the current source (*i.e.*, *p2*), the potential was 57.6 and 244.3 mV for the CE and the PEIW, respectively (*see* top right panels of Figs. 3Aii and 3Cii). Remarkably, the potential generated by the PEIW was ∼4.2 and ∼2.9 times greater than those of the CE and the PE, respectively.

We also plotted equipotential lines to visualize the spatial attenuation of electric stimulation (white solid lines of Figs. 3Ai, 3Bi, and 3Ci). Compared to the CE (Fig. 3Ai) as well as the PE (Fig. 3Bi), the PEIW exhibits denser equipotential contours (Fig. 3Ci), indicating a better confinement. The top views of the electrical potentials at the various vertical distances from the current source (Figs. 3Aii, 3Bii, and 3Cii) clearly shows a superior performance of the PEIW among the three electrodes for lateral confinement of the electric field which is required for high resolution prosthetic vision. Also, the potential decreased more drastically in the vertical direction with the PE and the PEIW (*i.e.*, vertically denser equipotential contours; compare Figs. 3Ai *vs.* 3Bi and 3Ci) suggesting they may be more effective than the CE in utilizing the anatomical laminar structure of the retina to specifically stimulate a certain layer (*see* Discussion).

We also characterized the potential changes as a function of current amplitude: 50, 100, 150, and 200 nA were applied to the current source (Fig.4). For the CE and the PE, the full width at half maximum (FWHM) values at the plane 2 μm away (*p2*) from the current source were constant regardless of the current amplitude: ∼12.1 and ∼25.7 μm (Figs. 3Ai and 3Bi), respectively. The potential of the CE seemed to be more confined because the FWHM was about a half of the FWHM of the PE. However, as shown in Fig. 3Ai, the electric field created by the CE spread much further vertically than those of the PE and the PEIW. Also, when 100 nA of current was applied, the maximum potential was weaker with the CE than the PE (59.2 and 84.7 mV, respectively). Although the FWHM values were not defined for the PEIW

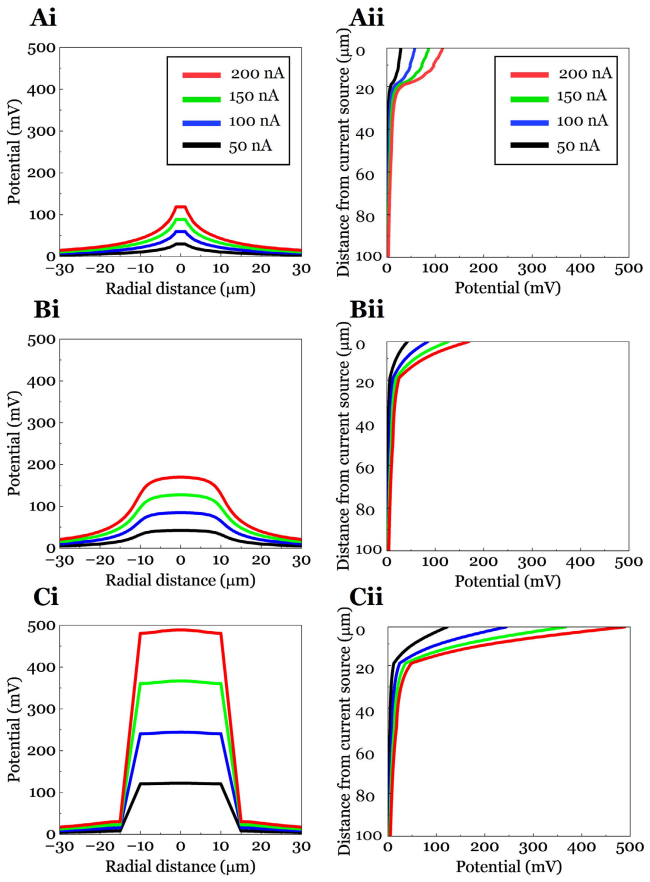

Fig. 4. For the same current, the potential magnitude of the PEIW was the strongest. **(Ai)** Potentials generated by the CE inserted in the middle INL were plotted as functions of the radial distance at a vertical distance of 2 μm from the electrode surface. Four different current amplitudes were shown. **(Aii)** Potentials were plotted as a function of the vertical distance from the current source. **(Bi** and **Bii)** Same as ***(Ai)*** and ***(Aii)*** but for the PE. **(Ci** and **Cii)** Same as ***(Ai)*** and ***(Aii)*** but for the PEIW.

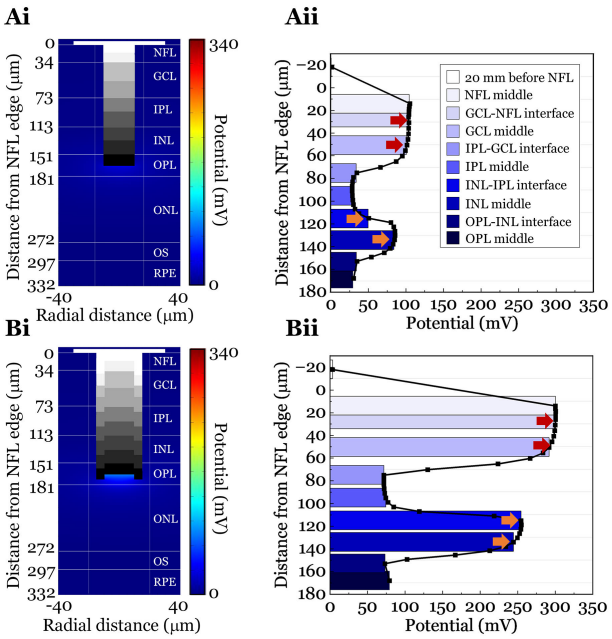

Fig. 5. The strength of the potential was the strongest when the electrode was inserted between the NFL and the GCL. **(Ai)** PE lengths when each electrode was inserted into 9 locations: GCL-NFL interface (white), GCL middle, IPL-GCL interface, IPL middle, INL-IPL interface, INL middle, OPL-INL interface, and OPL middle (black), respectively. **(Aii)** Maximum potential plot of PEs as a function of the location of the current source. Color-coded bar graphs show simulation results of the 9 locations; data points on a solid show the potential values measured from more locations. A disk electrode was also placed 20 μm away from the VB-NFL interface (shown at top of the plot) to show the difference between potentials created by a planar and penetrating electrode. **(B)** Same as ***A*** but for PEIWs.

because the potential could not be measured at the *p2* due to an insulating wall, the spread of the PEIW was apparently well confined within its electrically active area. Therefore, the effective FWHM can be further reduced with a much smaller pillar diameter, promising an even better spatial confinement.

We also plotted potential changes as a function of vertical distance from the current source (Figs. 4Aii, 4Bii, and 4Cii). Consistent with the trend of the equipotential contours (Figs. 3Ai, 3Bi, and 3Ci), the potential of the PEIW dropped faster with the distance than those of the CE and the PE. This result also confirms better stimulation confinement in the vertical direction.

B. The Strongest Potential Was Measured When the Electrodes Were Placed Inside the NFL and the GCL

In order to examine maximum potential changes as a function of insertion depth, we varied the vertical position of the electrode surfaces (Fig. 5) in the PE and PEIW configurations because they showed better electric field confinement in the vertical direction (Figs. 3Ai, 3Bi, and 3Ci). The electrodes were placed at 9 locations (bar graphs and their legends in Figs. 5Aii and 5Bii): OPL middle, OPL-INL interface, INL middle, INL-IPL interface, IPL middle, IPL- GCL interface, GCL middle, GCL-NFL interface, and NFL middle. For better granularity to determine the optimum, four additional measurements were taken between each layer (data points in the line graphs of Figs. 5Aii and 5Bii). In both designs, the potentials were the highest when the electrodes were placed at the NFL middle, and similarly much higher at the depths between the NFL middle and GCL middle layers (marked with red arrows in Figs. 5Aii and 5Bii) than other locations. Interestingly, it was confirmed that the potential values were substantially reduced when the electrodes were moved outside of the NFL and the GCL: for example, the potentials in the middle of the GCL were much larger than those in the middle of the INL. More importantly, when we located a disk electrode in VB to compare with the results from the PE and the PEIW, the potential values measured at 2 μm perpendicularly away from the current source were only ∼1.4 and ∼3.5 mV with the PE and the PEIW respectively. These results clearly indicate that it is more efficient to stimulate with a penetrating electrode (*i.e.*, PE and/or PEIW) inserted precisely into a desired location rather than to stimulate from the epiretinal surface. Also, it is worth to note the maximum value for the PEIW was about 3 times larger than for the PE (*compare* Figs. 5Aii and 5Bii). Taken all together, it may be most efficient for direct activation of retinal ganglion cells (RGCs)

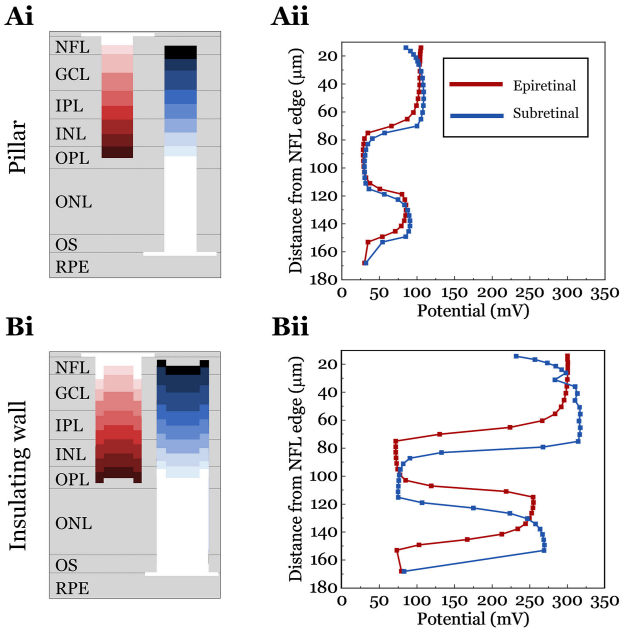

Fig. 6. Simulation results of maximum potentials generated by the PE and the PEIW inserted from subretinal *vs.* epiretinal sides were largely similar. **(Ai)** We schematically drew the appearance of PEs for both epiretinal and subretinal insertions. For both directions, electrodes were shown for the nine locations from the outer plexiform layer (OPL) to the ganglion cell layer-nerve fiber (GCL-NFL) interface **(Aii)** Maximum potential plot as a function of the location of the current source. Red and blue graphs represent the values for the epiretinal and the subretinal cases **(Bi and Bii)** Same as ***(Ai) and (Aii)*** but for the PEIW.

(*see* Discussion) to place the current source plane of the PEIW inside the NFL and the GCL.

It is important to note that there is another local maximum at the INL middle and/or the INL-IPL interface (marked with orange arrows in Figs. 5Aii and 5Bii). Targeting these locations would be beneficial for indirect activation of RGCs by stimulating bipolar cells (BCs) (*see* Discussion). Sharp reduction of the potentials outside these layers suggests that accurate placement is critical for indirect activation as well.

C. Epiretinal Stimulation vs. Subretinal Stimulation

We also compared results of epi- *vs.* sub-retinally inserted electrodes in the two designs by plotting potentials as a function of insertion location (Fig. 6). The results showed that the patterns of potential change were largely similar for the PE and PEIW designs, and the vertical offset between epi- and sub-retinally inserted electrodes was minute with the PE (*compare* the red and blue curves in Figs. 6Aii and 6Bii). As and example of the similarity, when a PE was inserted into the middle region of the INL layer (*i.e.*, 166 μm away from the NFL in the subretinal direction), the maximum potential values measured at a position of 2 μm away from the current source were ∼84.6 and ∼84.8 mV for the subretinal and the epiretinal cases, respectively (Fig. 6Aii). In contrast, the potential plots of the PEIW design showed a much larger offset between the epiretinal *vs.* subretinal results although overall shapes appeared similar (Fig. 6Bii). These offsets were caused by the different layers the current source faces in different directions of insertion. As each layer had different thickness and conductivity, different insertion directions at the same location would have resulted in dissimilar outcomes. The PEIW showed a larger offset potentially due to the unique physical barrier limiting the effects of layers opposite to the side faced by the current source, resulting in a better directionality of stimulation.

D. Visualization of the Estimated Quality of Artificial Vision

To visualize differences in the estimated quality of artificial vision, we additionally simulated with 5 by 5 arrays for the PE and the PEIW (Fig. 7); the electrode surfaces are 20 μm in diameter and the center-to-center distance between neighboring electrodes is 80 μm. We first compared the potential differences between the PE and the PEIW arrays with their current sources placed at the INL middle.

When some electrodes were activated to resemble a letter 'K', the PEIW showed a stronger electric stimulus and better spatial confinements (Figs. 7A and 7B), promising a higher-resolution electric field for prosthetic vision. The maximum potential values of the PE were 12.8, 8.9, and 6.2 mV at 0, 5, and 10 μm away from the current source, respectively (right panels of Figs. 7Aii-7Aiv). In contrast, the maximum values of the PEIW were 29.8, 20.1, and 12.2 mV at 0, 5, and 10 μm away from the current source, respectively (right panels of Figs. 7Bii-7Biv). We also tested another insertion in GCL middle for the PEIW (Fig. 7Ci), and found that the maximum potentials were 35.6, 24.3, and 15.2 mV at 0, 5, and 10 μm away from the current source (Figs. 7Cii-7Civ).

Lastly, we plotted the potential values at the three locations over the five current-carrying electrodes (across the white dotted line shown in the top left panel of Fig. 8A). Overall, the PEIW created stronger potentials than PE did (Figs. 8Ai, 8Aii, and 8Aiii).

IV. Discussion

A. Clinical Implications of This Simulation Study

In previous clinical trials, planar disk electrodes have demonstrated limited performance [5], [11], [13], [14], [15], [16], [18], probably due to poor spatial confinement of electric stimulation. To address this issue, there has been recent efforts to introduce 3D penetrating microelectrodes in retinal prosthetic applications [29], [30], [53], [54], [55]. Given the fragile and delicate property of the retina, penetrating electrodes may have challenges during and after the implantation. Interestingly however, a recent clinical testing with epiretinal implantation of an array of microneedle electrodes reported no adverse effect [29] such as bleeding and retinal detachment. This suggests risks associated with electrode penetration may be somehow manageable [29] while previous studies reported the benefits of 3D microelectrodes including lower stimulation threshold [27], [29] and more specific stimulation of target cell types [30], [31].

In the present study, to find more effective stimulation electrode design, we simulated spatial distribution of electrical potentials created by CE, PE, and PEIW electrodes.

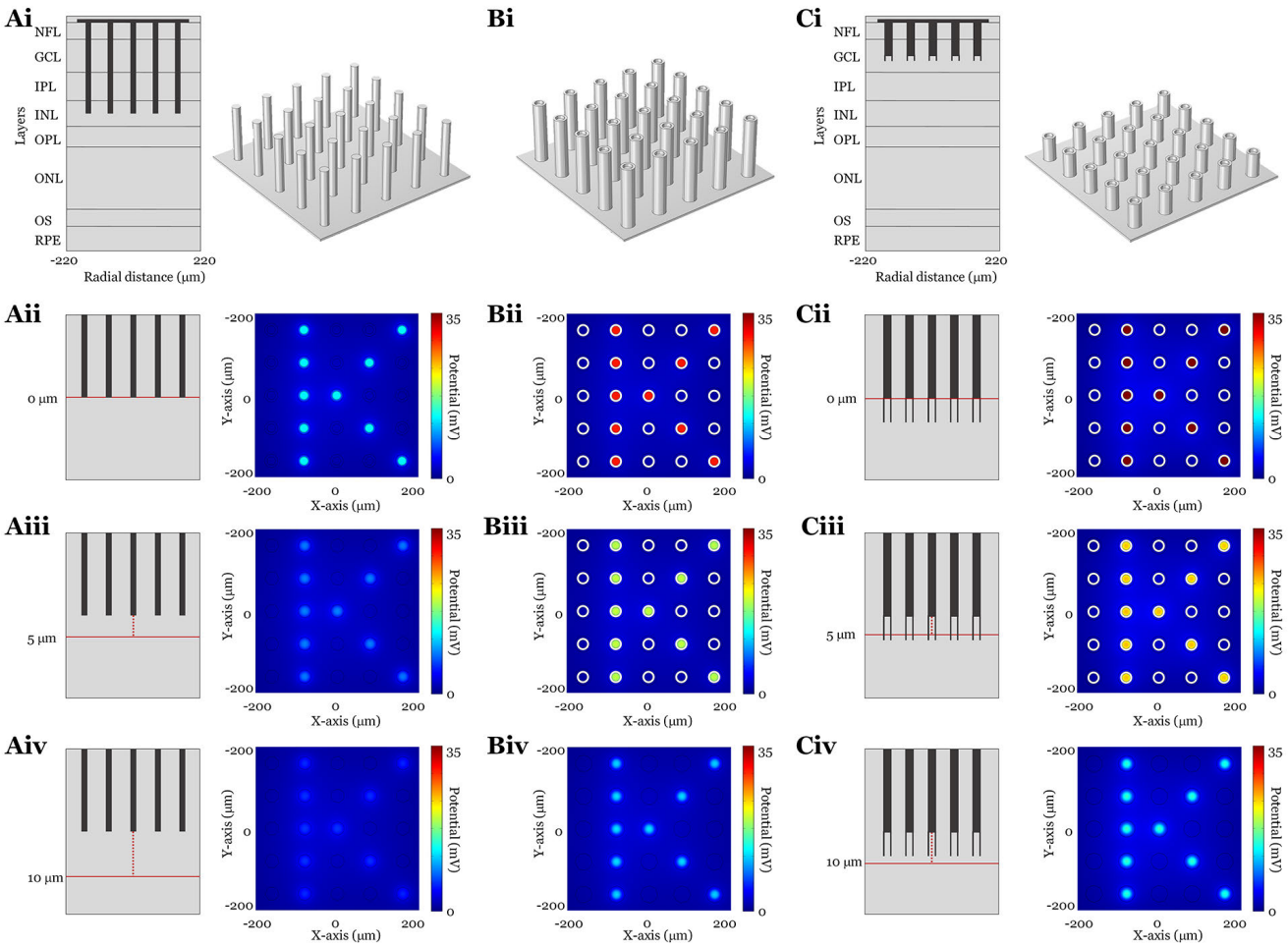

Fig. 7. Simulations with arrays of 5 × 5 electrodes demonstrate the letter "K" appear most clearly when the PEIW was inserted at the GCL middle position. **(Ai)** Cross-sectional and tilted views for the array electrodes placed in the INL middle. **(Aii-Aiv)** Among the 25 electrodes, 10 electrodes were active to represent the shape of K. Electrical potentials were characterized at distances of 0 μm ***(Aii)***, 5 μm ***(Aiii)*** and 10 μm ***(Aiv)*** away from the current source plane. The figure on the left depicts an enlarged view of only the INL layer after the insertion of electrodes. The top layer represents the IPL-INL interface, while the bottom layer represents the INL-OPL interface. **(B)** Same as ***A*** but for the PE. **(C)** same as ***B*** but for the insertion depth of the GCL middle. For **(*Cii-Civ*)**, The figure on the left depicts an enlarged view of only the GCL layer after the insertion of electrodes. The top layer represents the NFL-GCL interface, while the bottom layer represents the GCL-IPL interface.

Our various analyses demonstrated the PEIW can generated the strongest potential (Figs. 3-8). In addition, in order to find the effective layers to stimulate in, we repeated our simulations for the PE and the PEIW placed at various intraretinal planes ranging from the OPL middle to the NFL middle (Fig. 5). The strongest potentials from both types of electrodes were measured inside the NFL and the GCL, and the second strongest potential were measured in the INL layer or at the INL-IPL interface (Fig. 5Aii and 5Bii). Our results suggest that inhomogeneous conductivities (probably, thicknesses as well) of all retinal layers should be appropriately considered to better estimate the spatial properties of electric stimulation.

We found that the electrical stimulation created the maximum potential when an electrode was located in the NFL and the GCL (marked with red arrows in Figs. 5Aii-5Bii); this region is quite close to the axon initial segments (AISs) of retinal ganglion cells (RGCs), which are known to be most sensitive to electric stimulation [56], suggesting it may be the most effective target location for direct activation of RGCs.

On the other hand, it is also notable that electrical potential was near local maximum at the INL-IPL interface/the INL middle (marked with orange arrows in Figs. 5Aii-5Bii): bipolar cells (BCs) also have AIS-like regions around those planes [57], making it to be efficient target for indirect activation of RGCs (*i.e.*, activation of BCs). Although the potential was smaller near the INL region than near the GCL region, the indirect activation is known to have benefits of eliciting more physiological (*i.e.*, natural) spiking activities in RGCs [58], [59], [60], [61], [62].

It has long been an important research question how to selectively activate either ON or OFF type of RGCs [58], [59], [63], [64], [65], [66], [67]. Given the fact that dendrites of those two RGC types are stratified at the distinct depths in the IPL (Fig. 9), each sublamina may be accurately targeted using the electrodes we simulated here, potentially improving the performance of retinal prostheses by more preferential activation of either ON or OFF pathway. However, it would be considerably challenging in the degenerate retinas in which

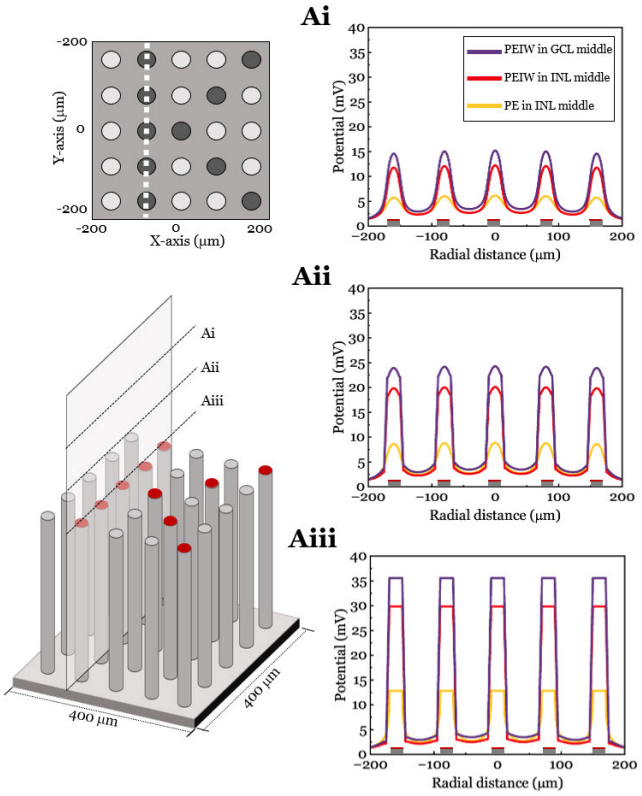

Fig. 8. Spatial distributions of electric potentials over five active electrodes in an array of 5×5 electrodes. The top left panel shows a top view of the array and the bottom left panel shows a bird's eye view of the array with the three measurement positions: **(Ai)** 10 μm, **(Aii)** 5 μm, and **(Aiii)** 0 μm away from the current source in the z-axis direction. Potential plots shown in ***Ai-Aiii*** were made along the dotted lines. Purple and red curves represent the potential distribution with PEIWs inserted in the middle of GCL and INL, respectively. Yellow curve shows the potential distribution with a PE in the middle of the INL.

the laminar structure is altered [68], [69]. Along with previous efforts of stimulation parameter optimization for the enhanced selective activation [58], [59], [63], [64], [65], [66], [67], the hardware approach such as the accurate positioning of penetrating electrodes may further advance discriminate activation of ON or OFF pathway.

B. Limitation of Our Study

Although we have used different conductivities of the heterogeneous retinal layers, those conductivity values were from the frog retinas [25], [34], [35], [36], [37], [38], [39], which have been most widely used in the retinal prosthetic modeling studies.

The lack of precise layer-by-layer conductivity information of the human retinas (or at least the non-human primate ones) would limit the translational significance of our study. Other limitations also include that we assumed the electrical properties are similar within each anatomical layer. For example, we assigned one conductivity to the OPL which comprises synaptic connections between photoreceptors and bipolar cells. However, electrical properties of each microscopic location may be different in the vertical direction depending on the synapses, potentially resulting in an anisotropic conductivity.

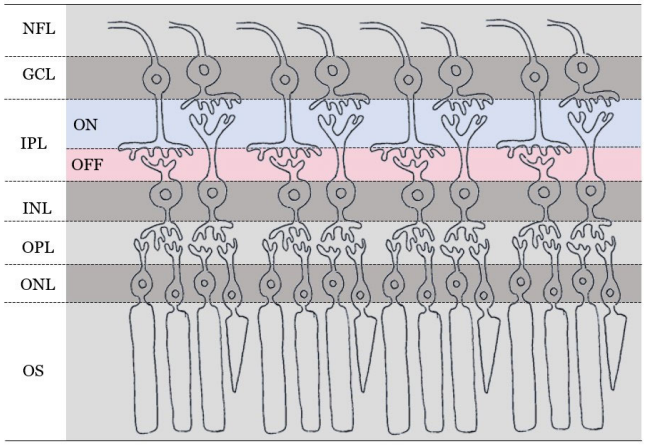

Fig. 9. ON and OFF types of retinal ganglion cells (RGCs) stratify their dendrites at the different depth in the inner plexiform layer (IPL). Those sublaminas are highlighted as light blue and pink horizontal bands.

However, the literature lacks such measurements, so we started with isotropic values. This limitation is expected to be easily overcome if reliable information becomes available, as our framework can readily accommodate anisotropic conductivities. Moreover, the retinal degeneration substantially alters not only RGC spiking patterns [68], [70] but also anatomical structures of the retina [68], [69], which is highly likely to change the spatial conductivity properties of the retina. Therefore, it is essential to precisely measure electrical conductivities of each retinal layers. We are planning to characterize the conductivities of different retinal layers of mice/rats which are the most widely used animal models for prosthetic researches.

It is also important to acknowledge that the present study included only computer modeling without *in-vivo/ex-vivo* experiments. As a result, some discrepancies between our findings and empirical outcomes may exist. For instance, in previous studies [71], BCs and RGCs have exhibited distinct sensitivities to electric stimulation (*i.e.*, extracellular potentials). Moreover, both classes (*i.e.*, BC and RGC) of retinal neurons are known to have numerous subtypes [72], [73]; their unique sensitivities and morphological differences should be considered in the numerical stimulations. Eventually, it would be imperative to test the penetrating electrode structures presented in our modeling study in *ex-/in-vivo* additional experiments and/or extra cellular-level simulations using NEURON [36], [74]. This comprehensive approach will provide a more accurate representation of the neural responses to electrical stimulation in the retina. Given the extreme variety of retinal degeneration level and pattern across individual patients, the most promising approach may be the use of high-resolution OCT or advanced technologies to accurately image the remaining retinal structure after degeneration in each subject. Then, we may recalibrate COMSOL simulations according to each individual's condition, thereby implementing personalized digital medicine.

Eventually, to be tested with actual retinal tissues, those penetrating electrodes must be developed. In particular, the insulating walls near the electrode tip in the PEIW design seem to be highly challenging to be fabricated but it can be formed

using a spacer lithography [75], [76]. Although the application of the PEIW may enable us to achieve high spatial resolution and efficient stimulation for better clinical outcomes, it may be also challenging to insert as well as immobilize electrodes at a precise depth within a thin retina.

REFERENCES

[1] C. A. Curcio, N. E. Medeiros, and C. L. Millican, "Photoreceptor loss in age-related macular degeneration," *Investigative Ophthalmol. Vis. Sci.*, vol. 37, no. 7, pp. 1236–1249, Jun. 1996.

[2] W. L. Wong et al., "Global prevalence of age-related macular degeneration and disease burden projection for 2020 and 2040: A systematic review and meta-analysis," *Lancet Global Health*, vol. 2, no. 2, pp. e106–e116, Feb. 2014.

[3] M. S. Humayun, E. De Juan, G. Dagnelie, R. J. Greenberg, R. H. Propst, and D. H. Phillips, "Visual perception elicited by electrical stimulation of retina in blind humans," *Arch. Ophthalmol.*, vol. 114, no. 1, pp. 40–46, Jan. 1996.

[4] J. F. Rizzo, J. Wyatt, J. Loewenstein, S. Kelly, and D. Shire, "Perceptual efficacy of electrical stimulation of human retina with a microelectrode array during short-term surgical trials," *Investigative Ophthalmol. Vis. Sci.*, vol. 44, no. 12, pp. 5362–5369, Dec. 2003.

[5] E. Zrenner et al., "Subretinal electronic chips allow blind patients to read letters and combine them to words," *Proc. Roy. Soc. B, Biol. Sci.*, vol. 278, no. 1711, pp. 1489–1497, Nov. 2010.

[6] A. K. Kiser and P. J. Pronovost, "Management of diseases without current treatment options," *J. Amer. Med. Assoc.*, vol. 301, no. 16, pp. 1708–1709, Apr. 2009.

[7] J. Wallber, "Audiologists' role in early diagnosis of Usher syndrome," *ASHA Leader*, vol. 14, no. 16, pp. 5–6, Dec. 2009.

[8] S. Y. Kim, S. Sadda, M. S. Humayun, E. de Juan, B. M. Melia, and W. R. Green, "Morphometric analysis of the macula in eyes with geographic atrophy due to age-related macular degeneration," *Retina*, vol. 22, no. 4, pp. 464–470, Aug. 2002.

[9] D. J. Margolis, G. Newkirk, T. Euler, and P. B. Detwiler, "Functional stability of retinal ganglion cells after degeneration-induced changes in synaptic input," *J. Neurosci.*, vol. 28, no. 25, pp. 6526–6536, Jun. 2008.

[10] R. J. Greenberg, T. J. Velte, M. S. Humayun, G. N. Scarlatis, and E. De Juan, "A computational model of electrical stimulation of the retinal ganglion cell," *IEEE Trans. Biomed. Eng.*, vol. 46, no. 5, pp. 505–514, May 1999.

[11] M. S. Humayun et al., "Interim results from the international trial of second sight's visual prosthesis," *Ophthalmology*, vol. 119, no. 4, pp. 779–788, Apr. 2012.

[12] M. S. Humayun et al., "Pattern electrical stimulation of the human retina," *Vis. Res.*, vol. 39, no. 15, pp. 2569–2576, Jul. 1999.

[13] A. K. Ahuja et al., "Blind subjects implanted with the Argus II retinal prosthesis are able to improve performance in a spatial-motor task," *Brit. J. Ophthalmol.*, vol. 95, no. 4, pp. 539–543, Sep. 2010.

[14] L. da Cruz et al., "The Argus II epiretinal prosthesis system allows letter and word reading and long-term function in patients with profound vision loss," *Brit. J. Ophthalmol.*, vol. 97, no. 5, pp. 632–636, Feb. 2013.

[15] A. Kotecha, J. Zhong, D. Stewart, and L. da Cruz, "The Argus II prosthesis facilitates reaching and grasping tasks: A case series," *BMC Ophthalmol.*, vol. 14, no. 1, p. 71, May 2014.

[16] K. Stingl et al., "Artificial vision with wirelessly powered subretinal electronic implant alpha-IMS," *Proc. Roy. Soc. B, Biol. Sci.*, vol. 280, no. 1757, Apr. 2013, Art. no. 20130077.

[17] T. Fujikado et al., "Evaluation of phosphenes elicited by extraocular stimulation in normals and by suprachoroidal-transretinal stimulation in patients with retinitis pigmentosa," *Graefe's Arch. Clin. Experim. Ophthalmol.*, vol. 245, no. 10, pp. 1411–1419, Mar. 2007.

[18] L. N. Ayton et al., "First-in-human trial of a novel suprachoroidal retinal prosthesis," *PLoS ONE*, vol. 9, no. 12, Dec. 2014, Art. no. e115239.

[19] D. Palanker, Y. Le Mer, S. Mohand-Said, M. Muqit, and J. A. Sahel, "Photovoltaic restoration of central vision in atrophic age-related macular degeneration," *Ophthalmology*, vol. 127, no. 8, pp. 1097–1104, Aug. 2020.

[20] D. Palanker, Y. L. Mer, S. Mohand-Said, and J. A. Sahel, "Simultaneous perception of prosthetic and natural vision in AMD patients," *Nature Commun.*, vol. 13, no. 1, p. 513, Jan. 2022.

[21] J. Jeong et al., "Liquid crystal polymer (LCP), an attractive substrate for retinal implant," *Sensors Mater.*, vol. 24, no. 4, pp. 189–203, 2012.

[22] J. H. Park, S. Shim, J. Jeong, and S. J. Kim, "A multi-photodiode array-based retinal implant IC with on/off stimulation strategy to improve spatial resolution," *JSTS, J. Semicond. Technol. Sci.*, vol. 17, no. 1, pp. 35–41, Feb. 2017.

[23] W. Tong, H. Meffin, D. J. Garrett, and M. R. Ibbotson, "Stimulation strategies for improving the resolution of retinal prostheses," *Frontiers Neurosci.*, vol. 14, p. 262, Mar. 2020.

[24] M. Djilas et al., "Three-dimensional electrode arrays for retinal prostheses: Modeling, geometry optimization and experimental validation," *J. Neural Eng.*, vol. 8, no. 4, Jun. 2011, Art. no. 046020.

[25] X. Cao, X. Sui, Q. Lyu, L. Li, and X. Chai, "Effects of different three-dimensional electrodes on epiretinal electrical stimulation by modeling analysis," *J. NeuroEng. Rehabil.*, vol. 12, no. 1, p. 73, Aug. 2015.

[26] T. Flores et al., "Optimization of pillar electrodes in subretinal prosthesis for enhanced proximity to target neurons," *J. Neural Eng.*, vol. 15, no. 3, Mar. 2018, Art. no. 036011.

[27] E. Ho et al., "Characteristics of prosthetic vision in rats with subretinal flat and pillar electrode arrays," *J. Neural Eng.*, vol. 16, no. 6, Oct. 2019, Art. no. 066027.

[28] T. Flores et al., "Honeycomb-shaped electro-neural interface enables cellular-scale pixels in subretinal prosthesis," *Sci. Rep.*, vol. 9, no. 1, Jul. 2019, Art. no. 10657.

[29] L. Yanovitch, D. Raz-Prag, and Y. Hanein, "A new high-resolution three-dimensional retinal implant: System design and preliminary human results," *BioRxiv*, Sep. 2022.

[30] S.-B. Shin et al., "Fabrication of a transparent array of penetrating 3D microelectrodes with two different heights for both neural stimulation and recording," *Sens. Actuators B, Chem.*, vol. 393, Oct. 2023, Art. no. 134184.

[31] P. Wang et al., "Direct-print three-dimensional electrodes for large-scale, high-density, and customizable neural interfaces," *BioRxiv*, Jun. 2023.

[32] P. Werginz, H. Benav, E. Zrenner, and F. Rattay, "Modeling the response of ON and OFF retinal bipolar cells during electric stimulation," *Vis. Res.*, vol. 111, pp. 170–181, Jun. 2015.

[33] P. Werginz and F. Rattay, "The impact of calcium current reversal on neurotransmitter release in the electrically stimulated retina," *J. Neural Eng.*, vol. 13, no. 4, Jun. 2016, Art. no. 046013.

[34] P. Werginz, B.-Y. Wang, Z. C. Chen, and D. Palanker, "On optimal coupling of the 'electronic photoreceptors' into the degenerate retina," *J. Neural Eng.*, vol. 17, no. 4, Aug. 2020, Art. no. 045008.

[35] Z. C. Chen, B.-Y. Wang, A. K. Goldstein, E. Butt, K. Mathieson, and D. Palanker, "Photovoltaic implant simulator reveals resolution limits in subretinal prosthesis," *J. Neural Eng.*, vol. 19, no. 5, Sep. 2022, Art. no. 055008.

[36] X. Song et al., "An in-silico analysis of electrically evoked responses of midget and parasol retinal ganglion cells in different retinal regions," *J. Neural Eng.*, vol. 19, no. 2, Mar. 2022, Art. no. 026018.

[37] C. J. Karwoski, D. A. Frambach, and L. M. Proenza, "Laminar profile of resistivity in frog retina," *J. Neurophysiol.*, vol. 54, no. 6, pp. 1607–1619, Dec. 1985.

[38] C. J. Karwoski, L. M. Proenza, and D. A. Frambach, "Determination of resistivity and transcellular current flow in frog retina," *Ann. New York Acad. Sci.*, vol. 481, pp. 365–368, Dec. 1986.

[39] E. Greenbaum and D. Zhou, *Implantable Neural Prostheses 1: Devices and Applications*. New York, NY, USA: Springer, 2009.

[40] S. A. Joarder, M. Abramian, G. J. Suaning, N. H. Lovell, and S. Dokos, "A continuum model of retinal electrical stimulation," *J. Neural Eng.*, vol. 8, no. 6, Oct. 2011, Art. no. 066006.

[41] M. Abramian, N. H. Lovell, A. Habib, J. W. Morley, G. J. Suaning, and S. Dokos, "Quasi-monopolar electrical stimulation of the retina: A computational modelling study," *J. Neural Eng.*, vol. 11, no. 2, Feb. 2014, Art. no. 025002.

[42] K. Loizos, A. K. Ramrakhyani, J. Anderson, R. Marc, and G. Lazzi, "On the computation of a retina resistivity profile for applications in multi-scale modeling of electrical stimulation and absorption," *Phys. Med. Biol.*, vol. 61, no. 12, pp. 4491–4505, May 2016.

[43] K. Loizos, R. Marc, M. Humayun, J. R. Anderson, B. W. Jones, and G. Lazzi, "Increasing electrical stimulation efficacy in degenerated retina: Stimulus waveform design in a multiscale computational model," *IEEE Trans. Neural Syst. Rehabil. Eng.*, vol. 26, no. 6, pp. 1111–1120, Jun. 2018.

[44] F. Shalbaf, N. H. Lovell, S. Dokos, M. Trew, and E. Vaghefi, "Foveal eccentricity can influence activation threshold in subretinal electrical stimulation," *Biomed. Phys. Eng. Exp.*, vol. 5, no. 3, Mar. 2019, Art. no. 035009.

[45] H. Kolb, E. Fernandez, and R. Nelson, *Webvision: The Organization of the Retina and Visual System*. Bethesda, MD, USA: National Library of Medicine, 2007.

[46] R. N. Fariss, Z.-Y. Li, and A. H. Milam, "Abnormalities in rod photoreceptors, amacrine cells, and horizontal cells in human retinas with retinitis pigmentosa," *Amer. J. Ophthalmol.*, vol. 129, no. 2, pp. 215–223, Feb. 2000.

[47] J. Wyatt and J. Rizzo, "Ocular implants for the blind," *IEEE Spectr.*, vol. 33, no. 5, pp. 47–53, May 1996.

[48] A. Y. Chow and V. Y. Chow, "Subretinal electrical stimulation of the rabbit retina," *Neurosci. Lett.*, vol. 225, no. 1, pp. 13–16, Mar. 1997.

[49] E. Zrenner et al., "The development of subretinal microphotodiodes for replacement of degenerated photoreceptors," *Ophthalmic Res.*, vol. 29, no. 5, pp. 268–280, 1997.

[50] E. Bloch, Y. Luo, and L. da Cruz, "Advances in retinal prosthesis systems," *Ther. Adv. Ophthalmol*, vol. 11, pp. 1–16, Jan. 2019.

[51] K. Gekeler et al., "Implantation, removal and replacement of subretinal electronic implants for restoration of vision in patients with retinitis pigmentosa," *Current Opinion Ophthalmol.*, vol. 29, no. 3, pp. 239–247, May 2018.

[52] C. Gargini, E. Terzibasi, F. Mazzoni, and E. Strettoi, "Retinal organization in the retinal degeneration 10 (rd10) mutant mouse: A morphological and ERG study," *J. Comp. Neurol.*, vol. 500, no. 2, pp. 38–222, 2007.

[53] H. Roh et al., "Fabrication of high-density out-of-plane microneedle arrays with various heights and diverse cross-sectional shapes," *Nano-Micro Lett.*, vol. 14, no. 1, pp. 1–19, Dec. 2021.

[54] D. Raz-Prag, R. Gefen, and D. Weinberger, "A newly developed surgical technique for epiretinal implantation of retinal prosthesis," *Investigative Ophthalmol. Vis. Sci.*, vol. 53, no. 14, p. 5522, Mar. 2012.

[55] L. Yanovitz, D. Raz-Prag, K.-O. Eden, R. Saini, Y. Hanein, and R. Gefen, "Retinal response evoked and recorded with 3D electrodes designated for a novel prosthetic device," *Investigative Ophthalmol. Vis. Sci.*, vol. 55, no. 13, p. 1808, Apr. 2014.

[56] S. I. Fried, A. C. W. Lasker, N. J. Desai, D. K. Eddington, and J. F. Rizzo, "Axonal sodium-channel bands shape the response to electric stimulation in retinal ganglion cells," *J. Neurophysiol.*, vol. 101, no. 4, pp. 1972–1987, Apr. 2009.

[57] T. Puthussery, S. Venkataramani, J. Gayet-Primo, R. G. Smith, and W. R. Taylor, "NaV1.1 channels in axon initial segments of bipolar cells augment input to magnocellular visual pathways in the primate retina," *J. Neurosci.*, vol. 33, no. 41, pp. 16045–16059, Oct. 2013.

[58] M. Im and S. I. Fried, "Spatial properties of network-mediated response of retinal ganglion cells to electric stimulation," in *Proc. 7th Int. IEEE/EMBS Conf. Neural Eng. (NER)*, Apr. 2015, pp. 256–259.

[59] M. Im and S. I. Fried, "Indirect activation elicits strong correlations between light and electrical responses in ON but not OFF retinal ganglion cells," *J. Physiol.*, vol. 593, no. 16, pp. 3577–3596, Jun. 2015.

[60] M. Im and S.-W. Kim, "Neurophysiological and medical considerations for better-performing microelectronic retinal prostheses," *J. Neural Eng.*, vol. 17, no. 3, Jun. 2020, Art. no. 033001.

[61] S. Kim, H. Roh, and M. Im, "Artificial visual information produced by retinal prostheses," *Frontiers Cellular Neurosci.*, vol. 16, Jun. 2022, Art. no. 911754.

[62] H. Roh, Y. Otgondemberel, and M. Im, "Short pulses of epiretinal prostheses evoke network-mediated responses in retinal ganglion cells by stimulating presynaptic neurons," *J. Neural Eng.*, vol. 19, no. 5, Sep. 2022, Art. no. 055006.

[63] P. Twyford, C. Cai, and S. Fried, "Differential responses to high-frequency electrical stimulation in ON and OFF retinal ganglion cells," *J. Neural Eng.*, vol. 11, no. 2, Apr. 2014, Art. no. 025001.

[64] J. H. Kang, Y. J. Jang, T. Kim, B. C. Lee, S. H. Lee, and M. Im, "Electric stimulation elicits heterogeneous responses in ON but not OFF retinal ganglion cells to transmit rich neural information," *IEEE Trans. Neural Syst. Rehabil. Eng.*, vol. 29, pp. 300–309, 2021.

[65] J.-I. Lee and M. Im, "Optimal electric stimulus amplitude improves the selectivity between responses of ON versus OFF types of retinal ganglion cells," *IEEE Trans. Neural Syst. Rehabil. Eng.*, vol. 27, no. 10, pp. 2015–2024, Oct. 2019.

[66] M. Im and S. I. Fried, "Temporal properties of network-mediated responses to repetitive stimuli are dependent upon retinal ganglion cell type," *J. Neural Eng.*, vol. 13, no. 2, Feb. 2016, Art. no. 025002.

[67] M. Im, P. Werginz, and S. I. Fried, "Electric stimulus duration alters network-mediated responses depending on retinal ganglion cell type," *J. Neural Eng.*, vol. 15, no. 3, Mar. 2018, Art. no. 036010.

[68] H. Roh, Y. Otgondemberel, J. Eom, D. Kim, and M. Im, "Electrically-evoked responses for retinal prostheses are differentially altered depending on ganglion cell types in outer retinal neurodegeneration caused by $Crb1$ gene mutation," *Frontiers Cellular Neurosci.*, vol. 17, Feb. 2023, Art. no. 1115703.

[69] B. W. Jones, R. L. Pfeiffer, W. D. Ferrell, C. B. Watt, M. Marmor, and R. E. Marc, "Retinal remodeling in human retinitis pigmentosa," *Experim. Eye Res.*, vol. 150, pp. 149–165, Sep. 2016.

[70] S. F. Stasheff, "Emergence of sustained spontaneous hyperactivity and temporary preservation of off responses in ganglion cells of the retinal degeneration ($rd1$) mouse," *J. Neurophysiol.*, vol. 99, no. 3, pp. 1408–1421, Mar. 2008.

[71] S. W. Lee, D. K. Eddington, and S. I. Fried, "Responses to pulsatile subretinal electric stimulation: Effects of amplitude and duration," *J. Neurophysiol.*, vol. 109, no. 7, pp. 1954–1968, Apr. 2013.

[72] T. Baden, P. Berens, K. Franke, M. R. Rosón, M. Bethge, and T. Euler, "The functional diversity of retinal ganglion cells in the mouse," *Nature*, vol. 529, no. 7586, pp. 345–350, Jan. 2016.

[73] K. Franke, P. Berens, T. Schubert, M. Bethge, T. Euler, and T. Baden, "Inhibition decorrelates visual feature representations in the inner retina," *Nature*, vol. 542, no. 7642, pp. 439–444, Feb. 2017.

[74] K. E. Kish, S. F. Lempka, and J. D. Weiland, "Modeling extracellular stimulation of retinal ganglion cells: Theoretical and practical aspects," *J. Neural Eng.*, vol. 20, no. 2, Mar. 2023, Art. no. 026011.

[75] Y.-K. Choi, T.-J. King, and C. Hu, "Nanoscale CMOS spacer FinFET for the terabit era," *IEEE Electron Device Lett.*, vol. 23, no. 1, pp. 25–27, Jan. 2002.

[76] Y.-B. Park, M. Im, H. Im, and Y.-K. Choi, "Superhydrophobic cylindrical nanoshell array," *Langmuir*, vol. 26, no. 11, pp. 7661–7664, May 2010.